



LAWRENCE
LIVERMORE
NATIONAL
LABORATORY

Density functional study of atomic arrangements in bulk, grain boundary, and stacking fault of CrMnFeCoNi high-entropy alloy

S. Kang, A. Tamm

August 16, 2022

Computational Materials Science

Disclaimer

This document was prepared as an account of work sponsored by an agency of the United States government. Neither the United States government nor Lawrence Livermore National Security, LLC, nor any of their employees makes any warranty, expressed or implied, or assumes any legal liability or responsibility for the accuracy, completeness, or usefulness of any information, apparatus, product, or process disclosed, or represents that its use would not infringe privately owned rights. Reference herein to any specific commercial product, process, or service by trade name, trademark, manufacturer, or otherwise does not necessarily constitute or imply its endorsement, recommendation, or favoring by the United States government or Lawrence Livermore National Security, LLC. The views and opinions of authors expressed herein do not necessarily state or reflect those of the United States government or Lawrence Livermore National Security, LLC, and shall not be used for advertising or product endorsement purposes.

Density functional study of atomic arrangements in CrMnFeCoNi high-entropy alloy and their impact on vacancy formation energy and segregation

ShinYoung Kang^{a+*}, Artur Tamm^{b,c+}

^a Materials Science Division, Lawrence Livermore National Laboratory, Livermore, CA 94550, USA

^b Physics Division, Lawrence Livermore National Laboratory, Livermore, CA 94550, USA

^c Present address: Institute of Physics, University of Tartu, Tartu 50090, Estonia

+ Contributed equally to this work

* Corresponding Author

Email: kang10@llnl.gov

Abstract

Using the density functional theory-coupled Monte Carlo approach, we explored the chemical short-range order (SRO) and element segregation in equimolar CrMnFeCoNi alloy. We found that state-of-the-art approximation of random element distribution is only applicable at > 1100 K close to the melting temperature, while the Cr-Cr repulsion driving the system stabilization and accompanying the formation of cubic Cr sublattice, and mild Ni-Ni attraction are the most prominent pair interactions at lower temperatures. Chemical potential and vacancy formation energy calculations indicate that Cr is most sensitive to the local chemical environment, making Cr atoms most stabilized when the preferred SRO is introduced. While the vacancy formation is predicted equally probable among five constituting elements in the random solid solution, Cr and Ni atoms show the lowest vacancy formation energies in the structure with SRO. Furthermore, distinct element segregation was predicted in the vicinity of planar defects, including symmetric tilt grain boundary and stacking fault, which we correlated to the site- and chemistry-dependent

atomic volume and bond lengths. It suggests that the local mechanical strain and bond energy induce the SRO development and element segregation: Namely, the system takes advantage of segregation of Ni atoms having large atomic volume or Cr-Cr pairs having elongated bond lengths to fill in the excess volume at defects that relaxes the mechanical strain field and optimizes bond energy distribution. The correlation between the SRO and properties of CrMnFeCoNi alloy needs further investigations, which is expected to greatly help understand and control the properties of high-entropy alloys.

Keywords

High-entropy alloy; Short-range order; DFT; Monte Carlo simulation; Segregation

1. Introduction

High-entropy alloy (HEA) [1] is a novel class of materials which consists of five or more principal elements and forms a solid solution in a single phase. The large number of different elements creates a significant configurational entropy component in the free energy of the material, which stabilizes, especially at elevated temperatures, the phase with a random elemental distribution throughout the sample. HEAs have been actively researched for various applications for extreme environments, such as nuclear fission, due to their improved strength, ductility, fracture toughness, resistance to hydrogen-embrittlement and radiation damage [2-5] compared to compositional elements making up the alloy. Furthermore, HEAs could be used in energy-related applications, such as catalysis and energy storage [6].

Cantor alloy [7] has been used as a model system for studying the properties of HEAs. It consists of five 3d transition metal elements: Cr, Mn, Fe, Co, and Ni, in equimolar ratio and forms a single-phase solid solution with a face-centered cubic (FCC) lattice. Studies have shown that the yield strength and tensile strength increase in the Cantor alloy when the temperature decreases [5, 8, 9], while the resistivity changes only slightly with the change in temperature [10]. More importantly, B. Gludovatz *et al.* reported the trade-off between strength and ductility/toughness was removed at cryogenic temperatures [11], opening a new avenue in controlling the

mechanical properties of metals and alloys. Also, it has been shown that it is possible to engineer the properties of the Cantor alloy by changing the ratio of Cr and Ni content [12], promising the design routes for HEAs with specific properties.

On the other hand, it is commonly assumed that HEAs form a random solid solution with no chemical short-range order (SRO), meaning that elements are randomly distributed throughout the sample making all lattice sites equivalent. The configurational entropy in HEAs is maximized in the case of an ideal mixing, which would drive the system to stabilize in a random solid solution. In several computational studies, random samples are realized by creating a special quasi-random structure (SQS) [13], which has been used to predict the properties of HEAs [14-19]. Recently, however, the evidence of SRO in these types of materials was reported using more extensive computational approaches [20, 21]. For example, A. Tamm *et al.* used the density functional theory (DFT) [22, 23] approach combined with Monte-Carlo (MC) [24] sampling (referred to as MC-DFT) and showed that the ternary and quaternary Ni-based CCAs have a relatively strong SRO signal [20]. Moreover, J. Ding *et al.* used calculations to show how the stacking fault energies are influenced by SRO in ternary CrCoNi alloys [21], and recent advancements in the experimental setup have made it possible to observe the SRO in the same material [25, 26], demonstrating the validity of the theoretical works. Using energy-dispersive X-ray spectroscopy (EDS), Q. Ding *et al.* [27] investigated the fluctuations in element distribution along a few atomic columns in Cantor alloy and CrMnFeCoPd. Although Cantor alloy has less prominent fluctuations in element distribution compared to CrMnFeCoPd, the authors warned to interpret their data for correlating to the SRO due to the lack of information on the arrangement of elements along each atomic column. To our knowledge, no experimental evidence for SRO in Cantor alloy is available. It can be either because the Cantor alloy is indeed a random solid solution, or due to the challenges to characterize the atomic-scale structure despite a few attempts using such as atom probe tomography, transmission electron microscopy, x-ray diffraction, neutron total scattering, and extended x-ray absorption fine structure techniques in general HEAs [25, 28-30]. Considering that the phase separation and dendrite formation have been observed in Cantor alloy during slow cooling [29] or additive manufacturing [31], however, it is worth to employ computational tools to provide useful insights into the atomic-scale

structure of Cantor alloy and the associated properties. In addition, the SRO could differ from bulk in the vicinity of larger defects, such as a grain boundary and stacking fault, as the various elements in the alloy are driven towards the defects differently. This could affect the HEA's mechanical properties when comparing alloys with different grain sizes. In fact, experimental work has shown that the yield strength increases if the grain sizes in the Cantor alloy are reduced [9]. This could be due to the larger interface area, but could also be influenced by changes in the SRO near the grain boundaries, such as element segregation to grain boundaries [32, 33].

A possible solution for more accurate description of atomic structures in HEAs is the stochastic simulation of atomic arrangements coupled with the DFT calculations to account for chemical, electronic, and magnetic interactions of elements. Therefore, by employing the MC-DFT method we studied the SRO in bulk crystalline Cantor alloy as well as its grain boundaries or stacking fault. Next, we calculated the chemical potentials in the bulk samples and used those to find the vacancy formation energies in both the SQS and SRO structures. Finally, we correlated the SRO and element segregation to the metallic radii and bond lengths between constituting elements, unveiling a part of the critical driving forces to the local chemical order.

2. Methods

DFT [22, 23] calculations were coupled with the MC [24] simulation to search for the equilibrium distribution of elements in CrMnFeCoNi alloy. A random solid solution structure, SQS [13], was generated as a starting structure of MC-DFT simulations at the MC temperature of 1500 K. Its final structure was carried over as a starting structure of successive MC-DFT simulations at the MC temperature of 1100 K, and the simulation continued in this manner until reaching the MC temperature of 300 K. We ignored the spin-polarization as CrMnFeCoNi alloy is paramagnetic under ambient conditions [34], and it also helps accelerating the exploration of the energy landscapes. For additional verification, however, we probed the energy state of predicted local chemical order in the presence of magnetic interactions and compared the energies from spin-polarized and non-spin-polarized calculations for a subset of MC-DFT simulation structures. It must be emphasized that within the computational resources available to the researchers,

reaching an equilibrium state with sufficiently large dataset was not possible, but still the number of MC steps was accessible enough to capture main trends as demonstrated by the agreement between MC-DFT predictions and experimental characterization [20, 21, 25, 26].

The DFT calculations were carried out using Vienna Ab initio Simulation Package (VASP) [35] with projector augmented plane-wave method [36] with 6, 7, 8, 9, and 10 valence electrons for Cr, Mn, Fe, Co, and Ni, respectively utilizing the Perdew-Burke-Ernzerhof (PBE) exchange-correlation functional [37]. In the first set of calculations for defect-free bulk supercells containing 256 atoms, an energy cutoff of 350 eV and Gamma point-only k -point sampling were employed for the MC-DFT, chemical potential and vacancy formation energy simulations. The lattice parameter was fixed to 3.52 Å. In the MC-DFT calculations, Fermi-Dirac smearing was used with the appropriate electronic temperature reflecting the MC simulation temperature, whereas the final point-defect calculations were carried out using Methfessel-Paxton smearing [38] with a smearing width of 0.2 eV. In these calculations, the ionic degrees of freedom were relaxed until the energy converged to $< 10^{-7}$ eV/atom. By performing additional calculations with the experimental lattice parameter of 3.6 Å [15] and a finer k -point grid ($2 \times 2 \times 2$ and $3 \times 3 \times 3$) for tens of selected element arrangements, we confirm that our MC-DFT simulation setting with Gamma-only k -point and 3.52 Å lattice parameter is still valid for obtaining reasonable chemical order and has little impact to the trends we observed in chemical SRO and vacancy formation energies (see Figs. S1 – S3).

In a second set of calculations containing grain boundaries or stacking fault, the lattice constant was fixed to the experimental value of 3.6 Å [15], while the atomic positions were fully optimized within the DFT until reaching $< 10^{-9}$ eV/atom energy convergence. Fermi smearing method with a smearing width of 0.06 eV was used along with an energy cutoff of 350 eV. Simulation cells of two symmetric tilt grain boundaries, $\Sigma 5$ (210)/[001] and $\Sigma 5$ (310)/[001], and stacking fault were constructed consisting of 480, 480, and 408 atoms, respectively. Sampling of k -points and detail of the simulation box dimensions can be found in Table S1, and the effect of k -point grids to the accuracy of the total energies can be seen from Fig. S1(b).

The chemical ordering of elements was quantified using the Warren-Cowley SRO parameter, α_m^{ij} [39, 40]:

$$\alpha_m^{ij} = 1 - \frac{y_m^{ij}}{c_i c_j}, \quad \text{eq. (1)}$$

where y_m^{ij} is the probability of finding the i - j pair in the m 's nearest neighbor shell, and c_i and c_j are the atomic concentration of type i and j , respectively. Random distribution of elements corresponds to $y_m^{ij} = c_i c_j$, resulting in $\alpha_m^{ij} = 0$. The upper bound of α_m^{ij} is 1, with maximal repulsion between i and j pairs, while α_m^{ij} becomes negative for attractive pairs.

The configurational entropy was calculated to estimate the free energy difference between SQS and a structure with non-zero SRO, using the cluster variation method (CVM) in the pair approximation[41]:

$$S_{\text{config}} = k_B \left\{ (z-1) \sum_i (c_i \ln c_i - c_i) - \frac{z}{2} \sum_{i,j} (y_1^{ij} \ln y_1^{ij} - y_1^{ij}) + \left(\frac{z}{2} - 1 \right) \right\}, \quad \text{eq. (2)}$$

where is k_B the Boltzmann constant and z is number of neighbors around a lattice site, which is 12 in FCC.

The chemical potentials of elements in the SQS and the structure with the SRO were calculated using a Widom-type substitution method [42] as used in the recent DFT studies of multicomponent alloys (see works by J. B. Piochaud *et al.* and C. Li *et al.* for more details) [16, 43]. An element A at a given site is substituted with another chemical element B, resulting in a total energy of system of $E_{A \rightarrow B}$, and $E_{B \rightarrow A}$ is the energy of system in the other way of substitution. Using the bulk supercell consisting of 256 atoms, total 256×4 substitutions were performed, as four substitution possibilities exist in the five-elements Cantor alloy. The energies of A to B substitution $\langle E_{A \rightarrow B} \rangle$ and B to A substitution $\langle E_{B \rightarrow A} \rangle$ averaged over multiple sites provide the chemical potential difference between elements A and B:

$$\mu_A^{\text{alloy}} - \mu_B^{\text{alloy}} = \frac{1}{2} (\langle E_{B \rightarrow A} \rangle - \langle E_{A \rightarrow B} \rangle). \quad \text{eq. (3)}$$

As we calculate the chemical potential differences for all sites in the 256-atom supercell together with the unperturbed system ($E = \sum_i N_i \mu_i$), the linear equations of our system are over-defined. Therefore, we report the chemical potentials for individual elements as well as the standard deviation for the errors.

Next, the vacancy formation energy was calculated using the DFT-calculated energies and the corresponding chemical potentials:

$$E_{\text{vac}}(V_A) = E_{\text{tot}}(V_A) - E_{\text{tot}}(\text{bulk}) + \mu_A, \quad \text{eq. (4)}$$

where $E_{tot}(V_A)$ and $E_{tot}(\text{bulk})$ are the total DFT energies of the system with and without vacancy of element A. This approach allows to evaluate the cost of removing an atom from the alloy and putting it into a reservoir representing the bulk HEA, which is closer to a realistic experimental setup of vacancy formation energy evaluation in HEAs.

Note that the choice of k-point grid and lattice parameter could significantly affect the quantitative accuracy of the system energies. Therefore, for the improving the accuracy of cohesive energies, chemical potentials, and vacancy formation energies, we sampled and recalculated a subset of structures with higher accuracy computational setting, which renders a constant energy shift for correction. This postprocessing procedure is described in more detail in Supplementary Material, and the correction energy is reported in Tables S2 and S3.

Finally, the computational analysis of the chemical potentials and vacancy formation energies was carried out with the GNU Octave software package [44]. The plots were created with the gnuplot software [45] and the atomic configurations were visualized using VESTA visualization tool [46].

3. Results and Discussion

3.1. Element distribution and chemical potentials in bulk

Starting from the SQS, the atomic arrangements were sampled at the MC temperature of 1500 K using MC-DFT simulations. After a few thousand steps we stopped the run, lowered the temperature to 1100 K and continued the simulation from the last step of the 1500 K. We repeated this approach multiple times at 900, 700, 500, and finally to 300 K to ensure reaching the low-energy state. Figure 1(a) displays the energy evolution as a function of MC steps at different MC temperatures. The energy was lowered at all temperatures by developing SRO parameters. Compared to the initial SQS, the final structure obtained from the MC-DFT simulation at MC temperature of 300 K is 50 meV/atom lower in energy. Decrease in energy attributes to the preferred chemical distribution presented by the SRO, demonstrating that bulk CrMnFeCoNi alloy is not a randomly ordered solid solution, and therefore SRO has to be taken into account when carrying out computational studies in CrMnFeCoNi alloy. The transition

temperature from random solid solution to local chemical order accounting for the entropic contribution will be discussed later in this article.

Although the MC temperatures are not physical quantities, the simulation data at different MC temperatures hint at the likeliness of the predicted SRO, as the MC temperature tunes the probability to overcome local energy barrier for site swaps. In agreement with R. Zhang *et al.*'s observation where the water-quenched CrCoNi alloy shows little SRO while the SRO parameters are promoted in the slow furnace-cooled samples [26], the SRO develops with temperature decrease as Fig. 1(b). The SRO parameter with value zero corresponds to a random distribution, while positive/negative values indicate repulsion/attraction in the pair. Same to the Cr-Cr repulsion reported in CrCoNi and CrFeCoNi alloys [20], we observe strong Cr-Cr repulsion and its magnitude increases with MC temperature decrease. In addition, interestingly, strong Ni-Ni attraction was predicted at low MC temperatures along with mild but obvious repulsion in Mn-Mn and Co-Co pairs at 300 K. The repulsion in Cr-Cr pair raises the probability to find Cr atoms paired with other elements, such as Cr-Co and Cr-Fe with negative SRO, while the probability to find Ni atoms neighboring with other elements is low with positive SRO due to the Ni clustering.

To elucidate the correlation between SRO development and system energy, we plotted the evolution of SRO parameters of Cr-Cr and Ni-Ni pairs in Fig. 1(c). Evolution of full lists of Cr- and Ni-containing pairs can be found in Fig. S4. Following the sum rule of SRO parameters, $\sum_j c_j \alpha_m^{ij} = 0$, the SRO parameter of the identical atoms' pair is related to the negative sum of SRO parameters of unlike pairs, according to $c_i \alpha_m^{ii} = -\sum_{j \neq i} c_j \alpha_m^{ij}$. For the Cr-containing pairs, the increase in α_1^{CrCr} occurs most significantly before reaching the 2500th MC step. In this period, while the decrease in α_1^{CrFe} and α_1^{CrCo} seems most relevant to the α_1^{CrCr} , the evolution of SRO parameters of Cr-X unlike pairs (X = elements other than Cr) over the MC steps is less prominent than that of α_1^{CrCr} as in Fig. S4(a). On the other hand, Fig. S4(b) shows a few noticeable changes in the α_1^{NiNi} coincide with the SRO development in the Ni-X unlike pairs (X = elements other than Ni). For example, the increase in α_1^{NiNi} at $\sim 1500^{\text{th}}$ and $\sim 3000^{\text{th}}$ MC steps accompanies the decrease in α_1^{NiMn} and α_1^{NiFe} , respectively. The dip in α_1^{NiNi} at $\sim 6000^{\text{th}}$ MC step occurs with the increase of α_1^{NiCr} , α_1^{NiCo} , and α_1^{NiFe} . It indicates that not the variations of the SRO of a single unlike pair is responsible to the overall decrease of α_1^{NiNi} during the MC-DFT simulations. Based on the

comparison of α_1^{CrCr} and α_1^{NiNi} with the SRO of their unlike pairs, we conclude that the interactions of unlike pairs collectively affect the Cr-Cr separation and Ni-Ni clustering.

Combining the evolution of SRO parameters with the mixing energy of binary alloys ΔH_{mix} , the critical pair interactions governing the system energy can be identified. Given that the mixing of Cr atoms with any heterogeneous elements is favorable with negative $\Delta H_{\text{mix}}(\text{Cr-X})$ as in Fig. S5, the attractions in Cr-X pairs contribute to the observed Cr-Cr separation and consequently the energy decrease in the system. As the $\Delta H_{\text{mix}}(\text{Ni-X})$ is negative for all unlike pairs at least for the non-spin-polarized calculations consistent to the simulation setting of our MC-DFT approach, Ni should preferentially pair with other than Ni atoms when the binary mixing is the primary driving force to the SRO development. Therefore, we conclude that the Ni-Ni clustering is less influenced by the chemical bonding energies of Ni-X unlike pairs and would not directly affect the stabilization of the system. Besides the chemical bonding, the Fermi surface instability can also drive the chemical SRO and lower the system energy, as the electronic density of states (DOS) of MC-DFT *ST-A* structure drops near to the Fermi level compared to SQS (Fig. S6). It is so-called the Fermi surface nesting mechanism [47]. Further study is demanded to prove this mechanism in Cantor alloy by predicting its electronic band structure and form of Fermi surface as in Ref. [48], which is beyond the scope of this work.

In addition to the SRO value in the first nearest-neighbor shell, the lattice was also inspected for possible appearance of long-range order, where Cr atoms occupy the corners of the cubic cell and other elements are at the face-centered lattice sites. The appearance of cubic Cr sublattice is clearly emerging in CrMnFeCoNi alloy as seen in the insets of Fig. 1(c) and the strong negative SRO value of Cr-Cr pairs in the second neighboring shell (Fig. S7). The simulated x-ray diffraction patterns of the Cr sublattice in the *ST-A* structure is compared with those of several ordered superlattice structures in FCC including DO_{22} , MoPt_2 , $L1_1$, and $L1_2$ (Fig. S8), and we confirm that the arrangement of Cr atoms in the *ST-A* structure is in a simple cubic lattice resembling the $L1_2$ phase, which was also experimentally characterized in CrCoNi alloy [49] and computationally predicted in CrFeCoNi alloy [50].

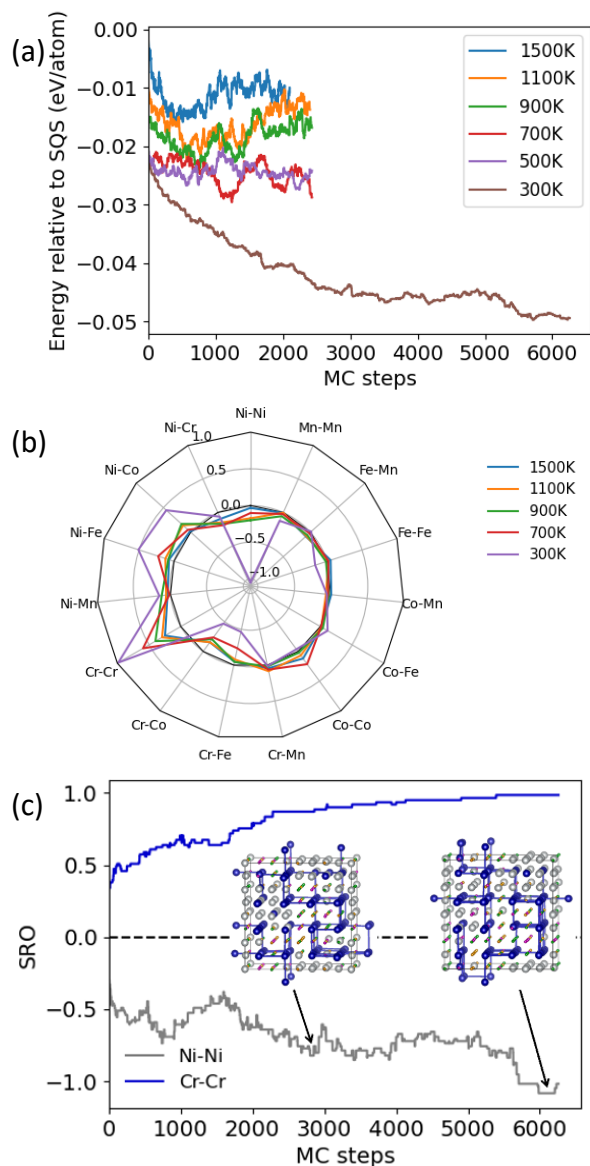


Figure 1. (a) Energy evolution of defect-free bulk CrMnFeCoNi alloy at different MC temperatures. The MC-DFT simulation started from the special quasi-random structure (SQS) at 1500 K, and the MC temperature is gradually lowered to 300 K. (b) Short-range order for the first nearest neighbors averaged over the last 500 MC steps from the MC-DFT approach. The SRO parameter with value 0 corresponds to a random distribution. (c) Evolution of SRO parameter for two selected atom pairs, Cr-Cr and Ni-Ni, at the MC temperature of 300 K. Insets show the atomic structures at two sampled MC steps, labelled *ST-A* and *ST-B*, displaying the formation of simple cubic sublattice of Cr atoms. Blue, purple, orange, green, and gray spheres represent Cr, Mn, Fe, Co, and Ni atoms. Ni and Cr atoms are enlarged to highlight their arrangements and Cr-Cr bonds are denoted by blue bars.

Two structures are taken at different states of MC simulations at 300 K for further analysis: one is at around the 3000th MC step and the other one near the end of the simulation at the 6000th MC step, which are labeled *ST-A* and *ST-B* respectively. The reason for this choice is purely due to the computational resources and the time constraints of the project. The *ST-A* was a local minimum at that point in time and it was selected for chemical potential and vacancy formation energy calculations. While these calculations were being performed, the MC-DFT simulation at 300 K was continued to gain confidence for the reached equilibrium state to > 6000th MC steps. The system evolved to an even lower energy state, *ST-B*, which is reported merely for comparison with *ST-A*. Besides, it must be emphasized that introduction of magnetism could change the ordering at lower temperatures, especially below 300 K, which will be investigated in a future publication. Despite that, we find that the Cr-Cr repulsion in HEAs is primarily chemical in nature (see the Supplementary Material for detail), while magnetism can intensify such Cr-Cr repulsion interactions [20, 51].

Table 1 summarizes the main bulk properties of the CrMnFeCoNi alloy in SQS, *ST-A* and *ST-B* states: the cohesive energy referencing to isolated metal elements in vacuum, configurational entropy as calculated following eq (2), mean-squared atomic displacement (MSAD), and transition temperature estimated from a simplified free energy model. The SRO development lowers the energy of the system, but at the same time it lowers the configurational entropy of the system, giving rise to a competition between the fully disordered system and the system with the SRO. Assuming a simplified free energy model ($F = E - T S_{\text{config}}$), we estimate that the random solid solution is stable at temperatures above 1147 K and the structure with strong Ni-Ni clustering (*ST-B*) appears below 396 K. For comparison, the melting temperature of the Cantor alloy has been estimated to be around 1500 K [9]. We observe that the configurations with SRO have a slightly lower lattice distortion as shown by MSAD, and is in similar order of magnitude with the experimentally measured value [52]. This is caused by the symmetry reduction of lattice sites in the crystal through the reordering of atomic pairs. In other words, lattice sites form groups with similar chemical environments that drives the system towards long-range order like crystal, for example, the $L1_2$ structure in Fig. 1(c).

Table 1. Cohesive energy (in eV), configuration entropy (in Boltzmann constant, k_B), mean-squared atomic displacement (MSAD, in pm^2), and estimated stability range of temperature (in K) of CrMnFeCoNi alloy in SQS, *ST-A* and *ST-B* structures.

system	E_{coh} (eV)	S_{config} (k_B)	MSAD (pm^2)	T range (K)
SQS	-4.377	1.608	62	$1147 \leq T$
<i>ST-A</i>	-4.420	1.173	48	$396 \leq T \leq 1147$
<i>ST-B</i>	-4.424	1.056	52	$T \leq 396$
Expt.			23.5 [52]	

Based on the initial SQS and low-energy *ST-A* MC-DFT structure, the chemical potential of constituting elements, μ_i^{alloy} , is calculated following eq. (3) and corrected using values in Table S2. The superscript *alloy* indicates the SQS or MC-DFT structure, and the subscript *i* refers to the element, Cr, Mn, Fe, Co or Ni. The calculated chemical potentials are referenced to the free energy of ground state pure elemental metal μ_i^0 , as $\Delta\mu_i^{\text{alloy}} = \mu_i^{\text{alloy}} - \mu_i^0$, enabling to see the relative stability of each element in the solid solution of CrMnFeCoNi alloy with respect to the elemental metal. The ground states of pure elemental metals are following BCC AFM Cr, BCC PM Mn, BCC FM Fe, HCP FM Co, and FCC FM Ni, where BCC = body-centered cubic, HCP = hexagonal close packed, AFM = anti-ferromagnetic, PM = paramagnetic, and FM = ferromagnetic.

The predicted $\Delta\mu_i^{\text{alloy}}$ in Table 2 shows that the solid solution of CrMnFeCoNi is metastable by 0.361 and 0.318 eV/atom in SQS and MC-DFT structure, respectively, compared to the pure elemental metals. Fe has the highest driving force to precipitate as an elemental metal (~ 0.517 eV/atom in SQS and ~ 0.486 eV/atom in MC-DFT structure). Interestingly, the range of $\Delta\mu_{\text{Cr}}^{\text{SQS}}$ is predicted from 0.230 to 0.280 eV in random solid solution CrCoNi, CrFeCoNi, and CrMnFeNi alloys [16, 53], which is comparable to our value in SQS. Given that the average chemical potentials of these alloys with respect to elemental metals ($\langle \Delta\mu_i^{\text{SQS}} \rangle$) are much lower than that of CrMnFeCoNi alloy with 0.077-0.113 eV/atom, the random solid solution of CrMnFeCoNi alloy offers less stable environments to elements other than Cr. On the other hand, the chemical

potential difference between SQS and MC-DFT structure, $\Delta\mu_i^{\text{MC-DFT}} - \Delta\mu_i^{\text{SQS}}$, shows that the SRO development significantly lowers the chemical potential of Cr. The sensitivity of Cr stability to the local environment in the CrMnFeCoNi alloy partly explains the experimental observations of Cr-rich precipitates or grain boundaries [33, 54, 55]. As Cr is often strategically added to prevent the alloys from degradation and radiation damage, careful design of microstructure and local environment should be considered to retain Cr in solid solution.

Figures S9 and S10 further display the impact of local chemistry to the total energy of the system when an atom is replaced with a different element. The linear regression of the MC-DFT structure indicates that all sites in the structure cannot be treated as equivalent. Since eq. (3) assumes all sites in the alloy are equivalent, as often assumed for HEAs, a bias is expected in the linear regression as there is not enough freedom in the equations to account for the site-dependent differences. In order to account for the SRO effect on the chemical potential, more advanced methods should be applied, such as quasi-chemical method or cluster variation method [56, 57], which is outside of the scope of current work and will be addressed in a later publication.

Table 2. Chemical potentials (in eV) with respect to that of pure metals in the SQS, $\Delta\mu_i^{\text{SQS}}$, and the *ST-A* structure obtained from the MC-DFT approach at 300 K, $\Delta\mu_i^{\text{MC-DFT}}$. The correction reported in Table S2 were applied (See the Supplementary Material for detail). The root mean-squared errors (RMSEs) are also provided.

Element	$\Delta\mu_i^{\text{SQS}}$	$\Delta\mu_i^{\text{MC-DFT}}$	$\Delta\mu_i^{\text{MC-DFT}} - \Delta\mu_i^{\text{SQS}}$
Cr	0.278	0.161	-0.117
Mn	0.329	0.316	-0.013
Fe	0.517	0.486	-0.030
Co	0.282	0.260	-0.022
Ni	0.399	0.366	-0.033
Avg.	0.361	0.318	-0.043
RMSE	0.097	0.119	

3.2. Vacancy formation energies in bulk

The vacancy formation energies in bulk CrMnFeCoNi alloy were calculated in both SQS and *ST-A* MC-DFT structure using eq. (4) with the corresponding averaged chemical potentials. Figure 2 depicts the vacancy formation energies at individual sites in the 256-atom simulation cell. In SQS, the energies vary around a single value of 2.43 eV, which is close to the value observed in the DFT study of CrMnFeNi alloy [16]. The standard deviation over all sites is 0.18 eV. Element-dependent average vacancy formation energies are summarized in Table S6. The lowest vacancy formation energy in SQS is 1.88 eV at a Co site. On the other hand, the vacancy sites in the MC-DFT structure with SRO are not equivalent, and the chemical elements differentiate the average vacancy formation energies. The average and standard deviation of vacancy formation energies are 2.25 ± 0.17 (Cr), 2.42 ± 0.19 (Mn), 2.58 ± 0.13 (Fe), 2.54 ± 0.13 (Co), and 2.28 ± 0.18 (Ni) eV. The average and standard deviation of vacancy formation energy over all sites is 2.41 ± 0.21 eV, slightly lower than in SQS and with a larger deviation. The lowest formation energy was found for a Cr site with a value of 1.71 eV. Despite the stabilization of Cr atoms aided by SRO, the less favored cohesive energy of Cr atoms leads to their low vacancy formation energies (Fig. S11).

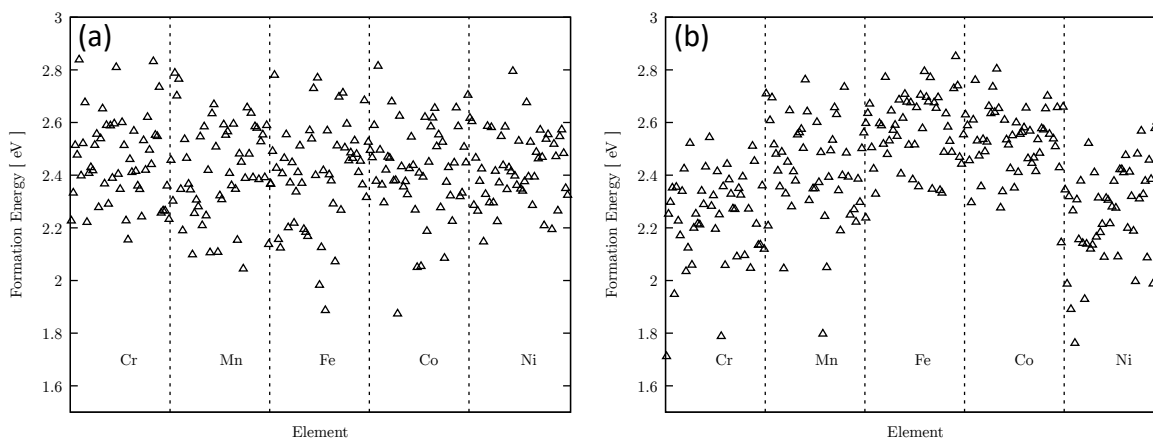


Figure 2. Vacancy formation energies sorted by chemical species in (a) SQS and (b) *ST-A* MC-DFT structure.

On average, the system with SRO will have higher vacancy concentrations than the SQS at a specified temperature, and most of the vacancy sites in the alloy will be at Cr and Ni sites, given that the vacancy formation energy and vacancy concentration in the dilute limit have the exponential relationship, $c(V_A) \sim \exp(-E_{vac}(V_A)/k_B T)$. The low formation energies of Cr vacancies are in agreement with the observation in CrFeCoNi alloy where the segregation of Cr into a Cr metal and/or Cr₂O₃ are expected combining with the lower migration energy barrier of Cr atoms [58]. E.-W. Huang *et al.* [59] reported the vacancy formation energy in the CrMnFeCoNi alloy as 0.64 eV at > 1000 K by combining Simmons–Balluffi methods, Seeger’s approach, Bichile and Kulkarni’s thermal expansion formulation, and positron annihilation lifetime spectroscopy. This value is much smaller than our calculated results, which can be attributed to three factors. First, our calculations ignore temperature-induced vibrational effects. At elevated temperatures the bond energies in a crystal are lowered and it becomes easier to create vacancies. Second, the experimental results show strong non-linear temperature dependence, implying that the vacancy formation energies at lower temperature could be much higher. Lastly, the bias in chemical potentials can overestimate the vacancy formation energies, by averaging over all sites and only distinguishing element types and not their neighborhoods. More accurate chemical potential calculations accounting for local chemical environments site-by-site may lower the vacancy formation energies.

3.3. Element distribution and segregation at grain boundaries

The MC-DFT approach was applied to predict element segregation and SRO parameters in two symmetric tilt grain boundaries (STGBs): $\Sigma 5$ (210)/[001] STGB where (210) as a grain boundary plane, [001] as a tilt axis, and 53.13° of a misorientation angle; and $\Sigma 5$ (310)/[001] STGB where (310) as a grain boundary plane, [001] as a tilt axis, and 36.87° of a misorientation angle. Hereinafter, the $\Sigma 5$ (210)/[001] STGB and $\Sigma 5$ (310)/[001] STGB are abbreviated as 210 STGB and 310 STGB, respectively. Structures of STGBs modeled in this study are displayed in the insets of Fig. 3(a) and (c). Due to the high computational cost of simulation, the MC-DFT simulation was performed only at the MC temperature of 700 K, which is high enough to avoid trapping at local minima, but low enough to develop SRO based on Fig. 1.

The grain boundary energy, GBE, is calculated as:

$$GBE = (E_{tot} - \sum_i N_i \mu_i^{\text{alloy}}) / 2A, \quad \text{eq. (5)}$$

where E_{tot} is the total DFT energy of the computational cell, N_i is the number of element i in the cell, and μ_i^{alloy} is the chemical potential of element i . The grain boundary plane area A is multiplied by two as each computational cell contains two grain boundary planes (depicted by vertical dashed lines in the insets of Fig. 3). For the choice of chemical potentials near to the grain boundary in eq. (5), both μ_i^{SQS} and $\mu_i^{\text{MC-DFT}}$ could be applied to represent two extreme cases from random solid solution to a low-energy SRO structure. Note that the resulting GBEs plotted in Fig. 3(a) and (c) are presented only for a guiding work, as the MC-DFT simulation was performed with the lower accuracy Gamma-only calculation setting and accordingly the μ_i^{SQS} and $\mu_i^{\text{MC-DFT}}$ values were used without the energy shifts. Further deviation of the chemical potentials in the vicinity of grain boundary from the $\mu_i^{\text{MC-DFT}}$ values is expected as the local chemical environments in bulk and near to defects would not be identical.

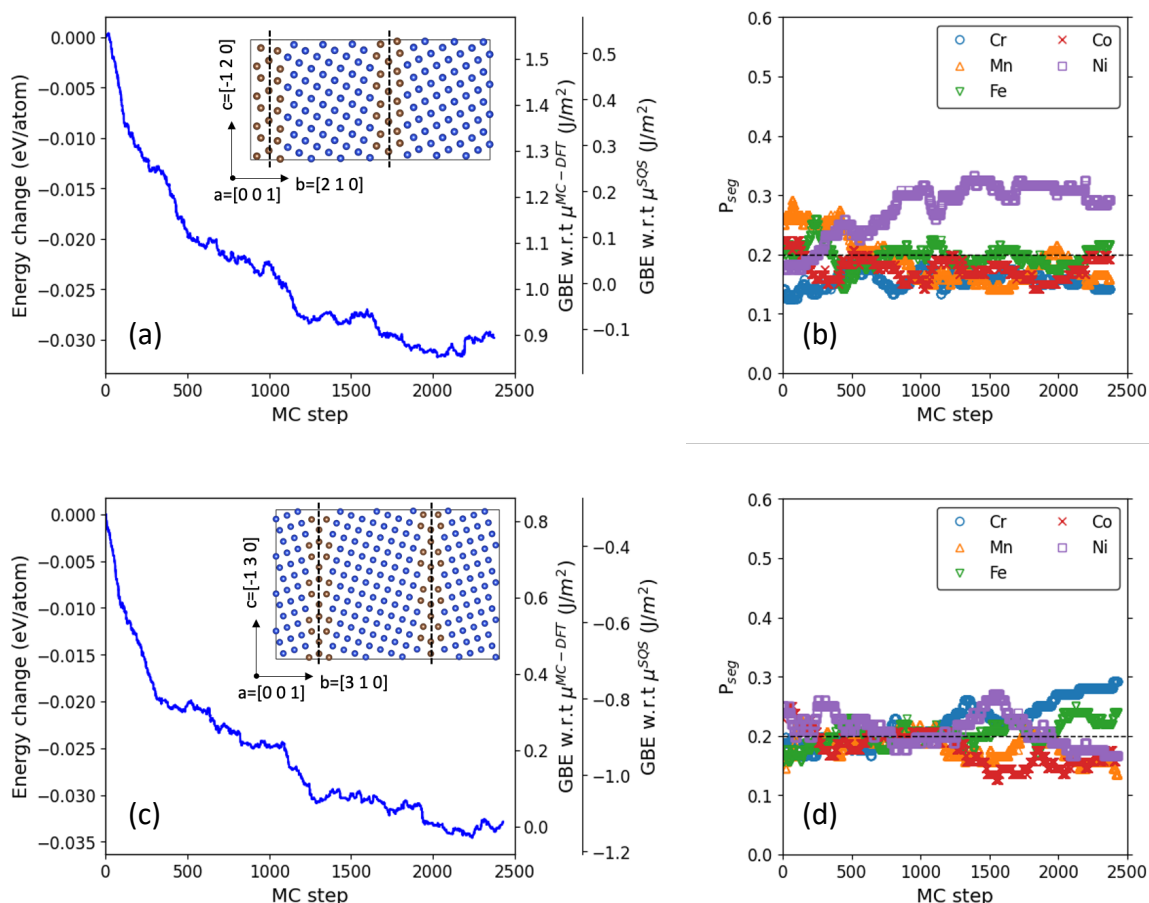


Figure 3. Evolution of (a, c) energy and (b, d) segregation probability at $\Sigma 5$ (210)/[001] STGB for (a) and (b); and $\Sigma 5$ (310)/[001] STGB for (c) and (d) as a function of MC steps. The MC-DFT simulation was performed at 700 K. The region where the segregation probability is calculated is denoted by brown spheres in the insets of (a) and (c).

The predicted GBEs are 0.5 and -0.3 J/m² for 210 STGB and 310 STGB respectively when elements are randomly distributed (referencing to μ_i^{SQS} values). Development of SRO and element segregation raise the GBEs to 0.9 and 0.0 J/m² for 210 STGB and 310 STGB (when referencing to μ_i^{MC-DFT} values) due to the decrease in chemical potentials. Note that the SRO in 210 and 310 STGBs may not be fully optimized to the low-energy states especially when accounting for the second or third nearest neighbors due to the small computation cell size in the presence of grain boundary. Therefore, the μ_i^{MC-DFT} values calculated from the 300 K bulk MC-DFT structure would be the lower bound, while the μ_i^{SQS} values serve as the upper bound:

$\mu_i^{\text{MC-DFT}} \leq \mu_i^{\text{at GB}} \leq \mu_i^{\text{SQS}}$. To estimate the uncertainty in $\mu_i^{\text{at GB}}$, we applied the Widom-type substitution technique to the atoms near the 210 STGB planes denoted by brown spheres in Fig. 3(a). On average, $\mu_i^{\text{at GB}}$ is 0.05 eV/atom higher than $\mu_i^{\text{MC-DFT}}$, corresponding to 0.22 J/m² decrease in the GBE compared to the ones referencing the $\mu_i^{\text{MC-DFT}}$ values. Interestingly, it suggests that the $\mu_i^{\text{at GB}}$ on the 210 STGB plane is similar to μ_i^{SQS} . Accurate prediction of site-dependent chemical potentials is challenging; Nevertheless, when comparing the relative magnitude between the GBE of 210 STGB with that of 310 STGB, the 310 STGB is more stable in agreement with other FCC metal cases, such as Al and Cu [60]. In both STGBs, the SRO and element segregation in MC-DFT structures lower the total energy more than 0.3 eV/atom, corresponding to 0.6-0.7 J/m² decrease in GBE.

The segregation probability of element i is calculated as $p_{\text{seg}} = N_i/N_{\text{GB}}$, where N_i is the number of element i atoms and N_{GB} is the total number of atoms near the grain boundary plane, which is noted by brown spheres in the insets of Fig. 3(a) and (c). The choice of grain boundary thickness is arbitrary, but we confirmed that it does not alter the observed trends. Evolution of p_{seg} shows strong Ni segregation to the 210 STGB as in Fig. 3(b). Segregation of Ni to the grain boundary is also found in recent experiments [32, 61]. Besides Ni segregation predicted for the 210 STGB in our study, favorable mixing enthalpy between Ni and Mn (Fig. S5) combined with high self-diffusivity of Mn [62, 63] can induce co-segregation of Ni and Mn at certain grain boundaries, rendering possibility of the NiMn phase formation observed in many experiments [29, 32].

On the other hand, until the GBE is lowered by ~ 0.6 J/m² at 1000th MC steps, there is no prominent element segregation to the 310 STGB as in Fig. 3(c-d). Between 1300th and 1700th MC steps, Cr and Ni co-segregation appears with mild Co and Mn depletion, and finally the structure evolves to Cr segregation followed by mild Fe segregation at 2500th MC steps. Cr segregation deprives Cr atoms from the grain interior, which further restricts the presence of Cr-Cr pairs in the first nearest neighboring shell. Interestingly, Cr segregation was also experimentally observed in the grain boundary regions especially where Ni and Mn are depleted and/or at higher temperatures [61, 64].

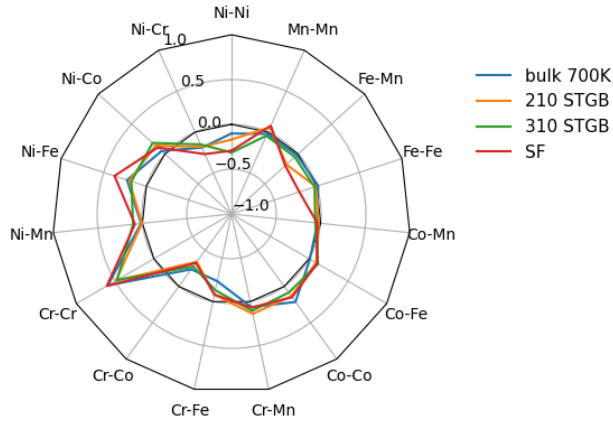


Figure 4. The SRO parameters averaged over the last 500 MC steps from the MC-DFT approach at the MC temperature of 700 K in bulk (blue line), $\Sigma 5$ (210)/[001] STGB (orange line, 210 STGB), $\Sigma 5$ (310)/[001] STGB (green line, 310 STGB), and stacking fault (red line, SF). The bulk SRO plotted here is the same as in Fig. 1(b) and is presented again for comparison only.

3.4. Element distribution and segregation at stacking fault

In the same manner to the STGBs, the element segregation and SRO parameters at stacking fault (SF) were assessed using the MC-DFT approach. Again, the MC-DFT simulation was performed at 700 K, the stacking fault energy SFE is calculated as

$$SFE = (E_{tot} - \sum_i N_i \mu_i^{\text{alloy}}) / A, \quad \text{eq.(6)}$$

and the segregation probability is calculated based on brown atoms in the inset of Fig. 5(a). From the SQS where the predicted SFE is -0.25 J/m^2 (referencing to μ_i^{SQS} values), at $\sim 4600^{\text{th}}$ MC step the total energy decreases by 35 meV/atom, and the SFE becomes 0.3 J/m^2 based on the $\mu_i^{\text{MC-DFT}}$ values. Similar to the GBEs, we are primarily concerned with how trends change with the local chemical environments not the computed quantities, as the SFEs were computed using the lower accuracy Gamma-only calculation setting. The SRO development and Ni deficiency are the dominant factors lowering the SFE (Fig. S12). The joint work combining experimental stacking fault probability with DFT-predicted elastic constants reported the SFE of CrMnFeCoNi alloy as $18.3\text{-}27.3 \text{ mJ/m}^2$ [15]. Again, it further demonstrates that μ_i^{SQS} and $\mu_i^{\text{MC-DFT}}$ are the upper and lower bounds of the chemical potentials of elements near to the defects, providing the ranges of

the GBE and SFE. The Widom-type substitution technique predicted that the average $\mu_i^{\text{at SF}}$ is 0.017 eV/atom higher than $\mu_i^{\text{MC-DFT}}$.

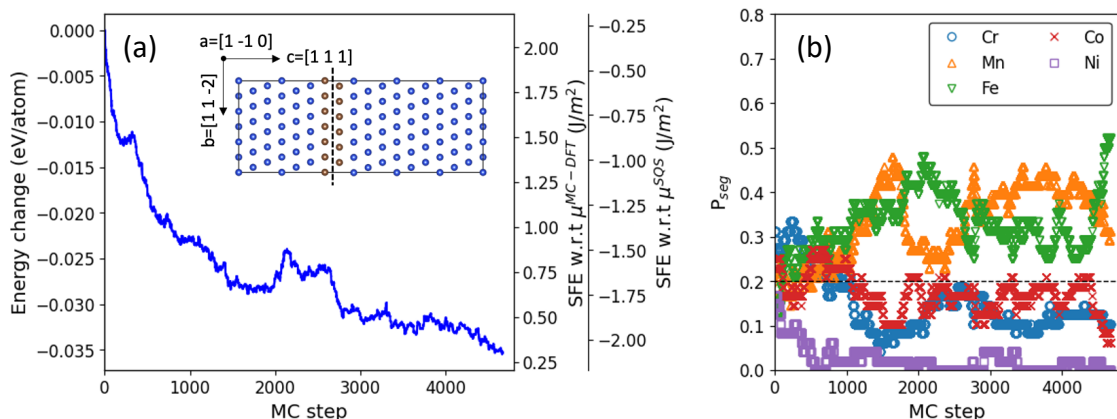


Figure 5. Evolution of (a) energy and (b) segregation probability at stacking fault as a function of MC steps. The region where the segregation probability is calculated is denoted by brown spheres in the inset of (a).

While STGBs and stacking fault share analogous SRO parameters indicated by strong repulsion in Cr-Cr pairs (Fig. 4), their element segregation behaviors are distinct: alternating Fe and Mn segregation along with significant Ni depletion was observed at the stacking fault (Fig. 5(b)). Ni deficiency is contrast to the 210 and 310 STGBs, suggesting dissimilar local environments between stacking fault and STGBs studied in this work. Such variations in the local environments can affect the precipitate and impurity nucleation, differentiating the mechanical response of materials. Given that low SFE materials are considered having high strength and increased ductility with enhanced twinning deformation, the segregation probability at low energy states can hint at an engineering strategy for improving mechanical properties of CrMnFeCoNi alloy. Indeed, A. J. Zaddach *et al.* suggested lower Ni and higher Cr compositions in the Cr-Mn-Fe-Co-Ni alloy to lower the SFE [15]. Less Ni in the overall composition would aid to reach the Ni-deficient local environment especially near to the SF, lowering the SFE.

Note that our MC-DFT simulations were performed without accounting for the spin-polarization, given that the CrMnFeCoNi alloy is paramagnetic with small saturated

magnetization of 1.34 emu/g under ambient conditions [34]. We confirmed the validity of our non-spin-polarized calculations for predicting the chemical ordering in bulk and defect supercells, by performing the spin-polarized DFT calculations (see the Supplementary Material for detail).

3.5. Factors affecting the chemical order and segregation

While the defect supercells exhibit the analogous SRO parameters to the bulk (Fig. 4), it is interesting to see that the element segregation varies depending on the defect types, *i.e.*, grain boundaries and stacking fault. We should caution, however, against overinterpretation of the trend, as the defect models we explored are limited to high-symmetric grain boundaries with small supercell dimensions, while there exist ample grain boundary structures with various misorientation angles and grain boundary planes. Although a statistical approach with multiple MC-DFT simulations is desired, several studies inform that the energy variation among multiple configurations at a certain chemical SRO (and vice versa) is smaller than the variation across chemical SRO parameters [21, 51]. It implies that the qualitative conclusions about the chemical order and segregation are relatively insensitive to the sample size of MC simulations. Therefore, we are primarily concerned with obtaining insights into the factors affecting the chemical order and segregation that can be generalized to other defect types and potentially other HEA systems.

Three factors were suggested affecting the local atomic arrangements: (i) local mechanical strain, (ii) bonding energy, and (iii) electronic and magnetic interactions [65]. Among these, L. Li *et al.* [32] attributed the GB segregation trend in the CrMnFeCoNi alloy to the mixing enthalpy of binary alloys. Based on the transmission Kikuchi diffraction and atom probe tomography analysis, the authors observed Ni segregation or Ni-Mn co-segregation accompanying Cr depletion at GBs, which could be rationalized by the negative mixing enthalpy in Ni-Mn pairs and positive mixing enthalpy in Ni-Cr pairs found from the THERMOCALC TCFE9 database via Ref. [32]. However, the mixing enthalpy of binary alloys obtained from DFT calculations does not show the same trend observed in the THERMOCALC TCFE9 database (see the Supplementary Material): namely, DFT calculations predict that Ni-Cr mixing is much more favorable than Ni-Mn mixing. More importantly, the mixing enthalpy alone, or the bonding energy in general, could not unravel the origin of observed Ni segregation, which was the basis of explaining the mixing enthalpy-driven

Ni-Mn co-segregation and Cr depletion in L. Li *et al.*'s study. In addition, the impact of mixing enthalpies of higher order systems, such as ternary, quaternary and quinary alloys, was found not deterministic to the stability of the Cantor alloy [66].

On the other hand, recent study by C. Li *et al.* reported that the metal element chemistry exhibits distinct compressive and tensile stress environments in random solid solution CrMnFeNi alloy [16], implying that the local mechanical strain would play an important role governing element segregation where the local excess free volume exists. Moreover, the strain field around the defects would be amplified due to the lattice mismatch near the defects and differences in the atomic radii. Also, looking at the defect-free bulk, the mean-squared atomic displacement in SQS is larger than the value in the MC-DFT structures (Table 1), implying that the fluctuations in local strains may be different in those structures. F. Cao *et al.* also observed the competition between mechanical strain energy and chemical bonding energy determining the element distribution near grain boundaries in CrCoNi alloy by explicitly computing the GB energies with and without structure relaxation [67], and similar phenomenon has been reported in other materials [68, 69]. Therefore, keeping the knowledge from the chemical bonding energy informed by the binary mixing enthalpies, we aim to understand the interplay between the distribution of local strain and element segregation.

Voronoi tessellation is geometry-based analysis not rooted in physical properties of materials. However, it is a useful tool to facilitate the analysis of local atomic structure [70, 71], and its variation as a function of composition allows to estimate the partial molar volume of elements [72]. On the other hand, the Voronoi volume at a certain fixed composition can inform the effective atomic radii, and thus we calculated the Voronoi volume of each site in the defect-free bulk supercell to elucidate the correlation between atomic radii and chemical SRO. Figure 6(a-b) and Table 3 display the average and spread of the Voronoi volume sorted by elements along with the molar volume of CrMnFeCoNi alloy, $7.024 \text{ cm}^3/\text{mol}$ when $a = 3.6 \text{ \AA}$, denoted by black dotted lines. In SQS, Cr and Ni atoms occupy larger volumes than the average value of $7.024 \text{ cm}^3/\text{mol}$, compensated by Mn and Fe atoms with smaller volumes. Undesired Cr-Cr bond and low probability of finding Ni-X bonds ($X = \text{other than Ni}$) widen the distribution of Voronoi volume for Cr and Ni atoms.

On the other hand, in the MC-DFT structure where Ni atoms cluster and Cr atoms separate from each other, Ni atoms significantly expand their territory by consuming the domain of Cr atoms and further shrinking the domain of Mn and Fe atoms. Now every single Ni site is larger than the molar volume of alloy, and the average atomic volume of Cr becomes smaller than that. Interestingly, the SRO reduces the standard deviation of Voronoi volume distribution in each element group, inferring that the less chemical homogeneity HEAs have, the more mechanical homogeneity can be achieved. The average and standard deviation of atomic volumes in CrMnFeCoNi alloy are summarized in Table 3 along with the molar volume of elemental metals.

The atomic volume can be related to the local atomic stress. C. Li *et al.* reported that Cr, Mn, and Fe atoms are under local compressive stress, while all Ni atoms are subject to local tensile stress in random solid solution CrMnFeNi alloy following their atomic number [16]. Similarly, in our study Cr, Mn, and Fe atoms experience volume contraction from SQS to the MC-DFT structure, while Ni atoms undergo expansion, demonstrating that the SRO relieves – at least partially – atomic stress and accordingly the local strain field. On the contrary, E.-W. Huang *et al.* reported tensile strain around Mn atoms in CrMnFeCoNi alloy using nano-projection X-ray microscopy measurement [59]. The discrepancy may be attributed to the elevated temperature over 1000 K where the self-diffusivity and volatility of Mn are high.

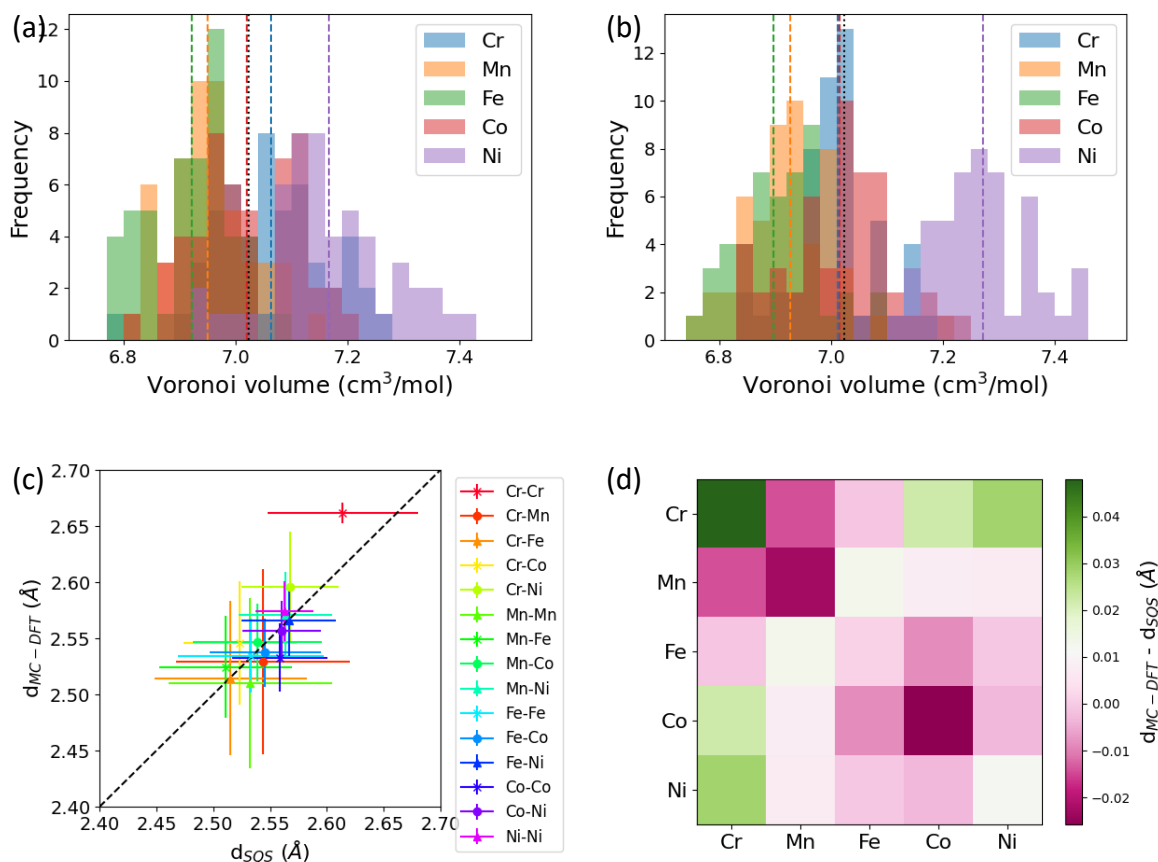


Figure 6. Voronoi volume distribution of each atom in 256-atoms bulk (a) SQS and (b) MC-DFT *ST-A* structure. Vertical dashed lines represent the average Voronoi volume of each chemical species and vertical dotted black line is the molar volume of the CrMnFeCoNi alloy, 7.024 cm³/mol. (c) Average bond lengths and (d) their difference between SQS and MC-DFT structure. Black dashed line in (c) is for guidance only.

Table 3. Average and standard deviation of Voronoi volume in cm³/mol of each chemical species. Percent changes with respect to the alloy's molar volume, 7.024 cm³/mol, are in parentheses.

Element	SQS	MC-DFT	Elemental metal
Cr	7.06 ± 0.10 (+0.6 %)	7.01 ± 0.07 (−0.2 %)	7.23
Mn	6.95 ± 0.07 (−1.1 %)	6.93 ± 0.08 (−1.4 %)	7.62
Fe	6.92 ± 0.08 (−1.5 %)	6.90 ± 0.09 (−1.8 %)	7.10

Co	7.02 ± 0.09 (−0.1 %)	7.02 ± 0.09 (−0.1 %)	6.62
Ni	7.17 ± 0.11 (+2.0 %)	7.27 ± 0.10 (+3.5 %)	6.59

Despite the valuable insights provided by the atomic volume into the relationship between chemical and mechanical homogeneity of the system, the Voronoi volume analysis is the mean field approximation averaged over the bonds with nearest neighboring 12 atoms in FCC. To better understand the impact of each bond component to local chemical order, the average and standard deviation of bond lengths for each element pair are plotted in Fig. 6(c) comparing the SQS and MC-DFT structure. Note that the bond length is one of the indicatives of the bond energy suggested by Y. Wu *et al.* [65]. The Cr-Cr bond length is exceptionally long compared to other pairs, reflecting the repulsion in Cr-Cr pairs. The SRO further elongates the Cr-Cr bonds from 2.61 Å to 2.66 Å and reduces the standard deviation of Cr-Cr bond lengths. Such elongation of Cr-Cr bonds is compensated by the low probability to find Cr-Cr pairs in the MC-DFT structure, leading to the net decrease in the Voronoi volume of Cr atoms. Data in the upper left domain, such as Cr-Cr, Cr-Ni and Cr-Co bonds, indicate the bond elongation upon the introduction of SRO, while the lower right domain, such as Co-Co and Mn-Mn bonds, is bond shrinkage, which becomes clearer looking at the difference in bond lengths between MC-DFT and SQS displayed in Fig. 6(d). Ni atoms have longer bond lengths in the MC-DFT structure when paired with Ni or Cr atom. While the average elongation of Ni-Ni bonds is as small as 0.012 Å from SQS to MC-DFT structure, the large number of Ni-Ni pairs present in the MC-DFT structure contributes to the net increase in the Voronoi volume of Ni atoms.

Note that in CrCoNi medium-entropy alloy, the partial molar volume follows the order of Cr >> Ni > Co [73], while the Voronoi volume in CrMnFeCoNi alloy shows the trend of Ni > Cr > Co in our calculations. The partial molar volume informs the alloy's volume changes upon the modification of alloy composition: For example, substitution of Ni with Cr increases the molar volume of $\text{Cr}_{1+x}\text{MnFeCoNi}_{1-x}$ ($0 < x \leq 1$) alloy. It can be presumably understood due to the higher probability of having longer Cr-Cr bonds. On the other hand, the variations in Voronoi volume in an ordered alloy lattice with a fixed composition rather characterize the minimization of strain field by displacing atoms from lattice sites. Indeed, the bond length variation for those 15 pairs

is 0.026 Å in SQS and 0.038 Å in the MC-DFT structure. Such an increase from SQS to the MC-DFT structure demonstrates that the diverse bond and strain energy is more correctly reflected in the MC-DFT structure, while the bond length and energy would be constrained in SQS. It further reinforces that the chemical inhomogeneity induced by SRO properly distributes the bond energies to obtain more homogeneous energy landscape and relaxation of strain field. The impact of atomic volume and bond length changes is expected to be amplified near the defects due to the increased degree of freedom such as free volume.

For the atomic volume analysis in the grain boundary or stacking fault systems, the Voronoi volume in the corresponding defect structure of single elemental metal is used as a reference to decouple the impact of chemical variety from the influence of defect. Accordingly, the spread in the x-axis direction in Fig. 7 is due to the structural defect, while the y-axis dispersion originates from the chemical variety in the system. Looking at the STGBs in single elemental metal, atoms closer to the grain boundary plane generally occupy larger volume due to the grain boundary excess volume, for example, creating a few discrete atomic volumes centered at 7.89, 7.54, 7.04, and 6.90 cm³/mol following the brown, red, cyan, and blue markers in 210 STGB (Fig. 7(a-b)). When multiple principal elements are randomly distributed in SQS (Fig. 7(a)), the spread of atomic volume is augmented, resulting in the range of atomic volume from 6.57 to 8.26 cm³/mol in 210 STGB. The local strain in the SQS with STGB is expected to be high especially near the GB plane due to the ignorance of element-dependent atomic volumes. On the contrary, the breadth of atomic volume in the MC-DFT structure is much narrower, from 6.61 to 8.08 cm³/mol (Fig. 7(b)). Combining with the histogram of atomic volume in the right panels of Fig. 7(a-b), one can find the relationship in the atomic volume, chemical element, and site in the defect structure. It clearly shows that the large atomic volume of Ni effectively compensates the excess volume at grain boundary in the MC-DFT structure. The average atomic volume of each chemical element depicted by horizontal dashed lines in the right panel of Fig. 7(b) becomes closer to the equilibrium atomic volume in bulk (Table 3), and thus -at least partial- release of local mechanical strain field is expected. It leads to the conclusion that the chemical inhomogeneity induced by SRO and element segregation enhances the homogeneity of mechanical strain in the MC-DFT structure.

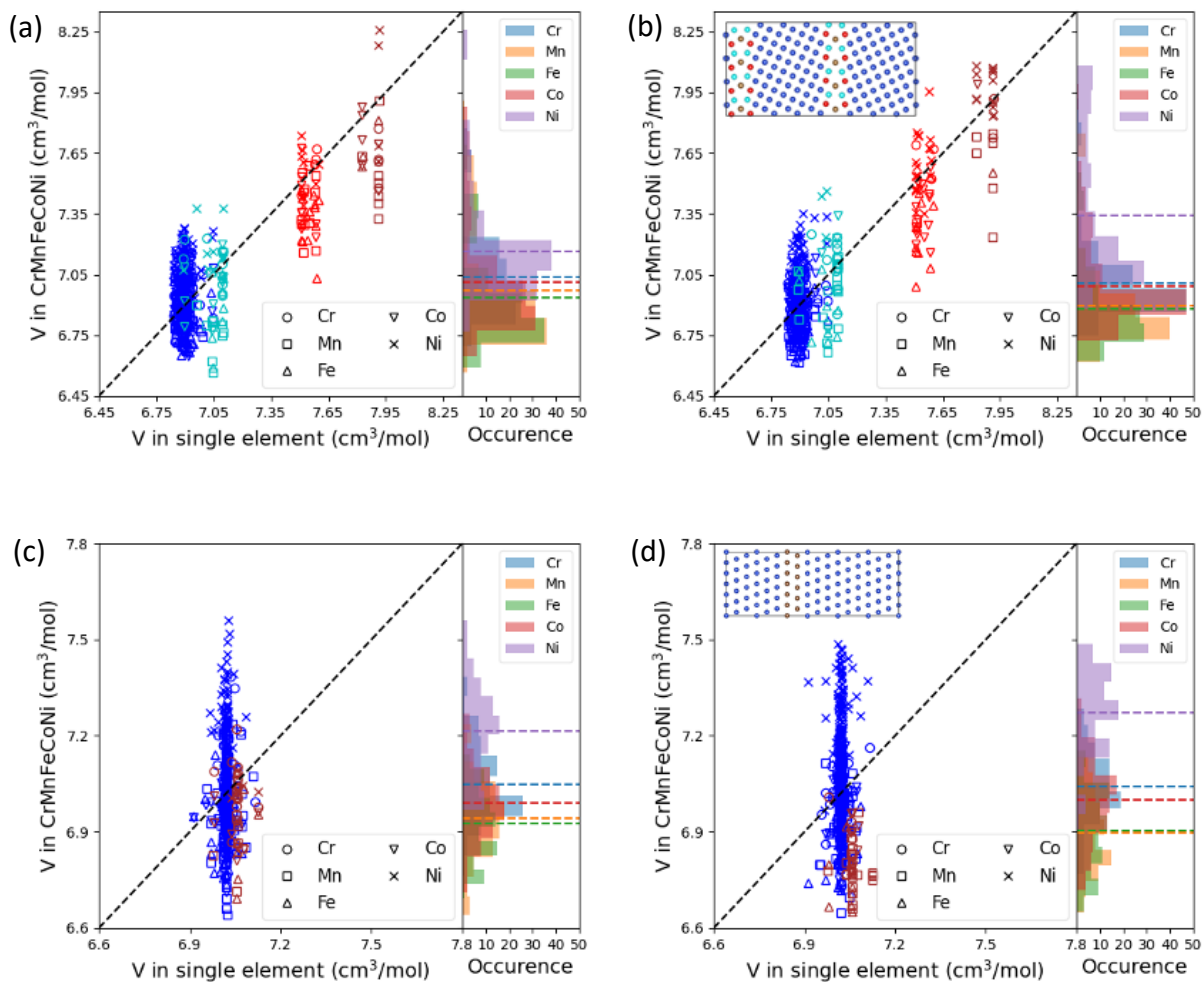


Figure 7. Voronoi volume distribution in the (a-b) 210 STGB and (c-d) stacking fault structures. (a, c) are from SQS and (b, d) are from the MC-DFT structures. Inset structures inform the color code of segregated atoms: Brown, cyan, red, and blue colors from the center of defect plane towards bulk interior. The Voronoi volume of element in the CrMnFeCoNi alloy is plotted in the y-axis and compared to that in single elemental metal with the same lattice constant plotted in the x-axis.

Similar analysis is applicable to the 310 STGB in Fig. S14. The main difference between 210 and 310 STGBs is that the grain boundary excess volume: In the single elemental metal without chemical variations (x-axis of Figs. 7 and S14), the largest atomic volume at 210 STGB is $7.91 \text{ cm}^3/\text{mol}$ corresponding to 112.7% of the metal's molar volume, while the largest atomic volume at 310 STGB is $8.54 \text{ cm}^3/\text{mol}$ corresponding to 121.6% of the metal's molar volume. As the excess volume in both STGBs is too large exceeding the equilibrium atomic volume in the bulk (Table 3), the predicted Cr segregation in 310 STGB can be a result of stochastic error from the Monte-Carlo simulation. If so, the Cr segregation may not be the only mechanism to compensate the large excess volume in 310 STGB to release the strain field. Or we also can hypothesize that the much larger excess volume in 310 STGB induces the elements with large atomic volume, *e.g.*, Ni, rather occupy the space away from the grain boundary plane than grain boundary segregation, mitigating the large excess volume near the grain boundary plane. Cr and Co are next largest elements in the MC-DFT structure (Table 3). When it comes to the mechanical strain energy as a driving force to segregation, both elements are eligible. However, only Cr segregation was observed in our simulation, indicating that other factors, such as chemical bonding energy, play a determining role to the element segregation besides the mechanical strain energy. Despite the quantitative comparison between mechanical and chemical energies is challenging in this multi-component alloy systems, our vacancy formation energies can hint at the interplay between the mechanical strain energy and chemical bonding energy, since a removal of an atom further imposes or releases the local strain field while removing several bonds with neighboring atoms at the same time. The average E_{vac} of Cr and Co in the MC-DFT structure is 2.25 (Cr) and 2.54 (Co) eV. Assuming the changes in strain energy would be comparable following their similar atomic volume, much higher average E_{vac} of Co implies that Co atom may have stronger bonds with neighboring atoms than Cr. The lower energy penalty associated with the strain and bonding energies would promote Cr segregation than Co. The alternating regions of Ni-Mn co-segregation and Cr segregation characterized in experiments at general high-angle GBs especially at higher temperatures [61, 64] support that the Cr segregation is a valid mechanism in certain conditions or grain boundary types, although further systematic study is demanded to clarify the transition from Ni segregation to Cr segregation.

Finally, the Voronoi volume and segregation trend at the stacking fault are compared. While the stacking fault in FCC materials shifts the sequence of layers, the coordination number of segregated atoms is the same to the atoms in bulk. Hence, the stacking faults offers negligible excess volume, narrowing the range of atomic volume to 6.91-7.13 cm³/mol in single elemental metal (x-axis in Fig. 7(c-d)). Chemical variety expands the range of atomic volumes to 6.64-7.56 cm³/mol in both SQS and MC-DFT structure. Larger atomic volume sites are dominant with Ni atoms and small atomic volume sites are occupied by Mn and Fe atoms, in agreement with the atomic volume trend in bulk (Table 3). Focusing on lattice sites near to the stacking fault (brown markers in Fig. 7(c-d)), segregation of Mn and Fe atoms to the stacking fault suggests that the tensile strain field near to the stacking fault is trivial, and thus atoms with large volume or long bond length such as Ni and Cr occupy regions away from the stacking fault. In summary, using Voronoi volume and bond length analysis as convenient but useful tools for local structure analysis, together with the chemical bonding energy we could successfully explain the predicted local chemical order and element segregation behaviors. Our findings support that the local strain field and bond energy play dominant, but competing roles determining the atomic-scale picture in HEAs. Further investigations on the role of electronic and magnetic interactions and quantification of relative importance among impacting factors are desired especially when considering HEAs in magnetic state.

4. Conclusions

Combining DFT calculations with the Monte Carlo approach, we predicted the distribution of chemical elements in CrMnFeCoNi alloy, which is otherwise challenging to probe experimentally. We found that the random atomic distribution in SQS CrMnFeCoNi is metastable by 0.3-0.4 eV/atom with respect to elemental metals of constituting species. Its energy can be lowered by > 50 meV/atom by introducing the SRO dominant with Cr-Cr repulsion and Ni-Ni attraction accompanied by the formation of $L1_2$ -type cubic Cr sublattice. The SRO development stabilizes the constituting elements by lowering their chemical potentials, but the impact was most significant for Cr due to its sensitive nature towards local environments. The chemical

inhomogeneity introduced by preferred SRO development also influences the vacancy formation energies, distinguishing chemical elements and sites. Unlike SQS where the similar local chemical environments lead to insignificant variations in vacancy formation energies, the MC-DFT structure is predicted to have high concentration of Cr and Ni vacancies. Our prediction on atomic arrangements is further expanded to the system with planar defects including $\Sigma 210$ and $\Sigma 310$ STGBs and stacking fault. The SRO predicted in defect-free bulk is equitably applicable to the defect systems, but interestingly, distinct segregation trend was predicted depending on the defect type: Ni segregation to $\Sigma 5$ (210)/[001] STGB, Cr segregation to $\Sigma 5$ (310)/[001] STGB, and co-segregation of Fe and Mn to stacking fault accompanied by Ni deficiency. A few experimental studies also reported segregation of Ni or Cr to grain boundaries in this alloy, supporting our prediction. We attribute the driving forces of the element arrangement to the strain field and bond energy based on the site- and chemistry-dependent analysis of atomic volume, bond length, and mixing enthalpy of binary alloys. We found that breaking the local chemical homogeneity by developing SRO helps relieving the local mechanical strain field and flattening the energy landscape. The consequences of atomic arrangements to the mechanical, chemical, and electronic properties of CrMnFeCoNi alloy demands further investigation, and we expect that our findings will be a valuable tool to understand and optimize materials properties by tuning the local chemical order in HEAs.

Acknowledgments

This work was performed under the auspices of the U.S. Department of Energy by Lawrence Livermore National Laboratory (LLNL) under Contract DE-AC52-07NA27344 and supported by the Laboratory Directed Research and Development Program at LLNL under the project tracking code 20-LW-015. In addition, A.T. was supported by the European Regional Development Fund and the programme Mobilitas Pluss (grant number MOBTP170). The authors appreciate Dr. Amit Samanta for providing grain boundary structures. The views and opinions of the authors expressed herein do not necessarily state or reflect those of the United States Government or any agency thereof. Neither the United States Government nor any agency thereof, nor any of their employees, makes any warranty, expressed or implied, or assumes any

legal liability or responsibility for the accuracy, completeness, or usefulness of any information, apparatus, product, or process disclosed, or represents that its use would not infringe privately owned rights.

References

- [1] J.W. Yeh, Y.L. Chen, S.J. Lin, S.K. Chen, High-Entropy Alloys – A New Era of Exploitation, *Materials Science Forum* 560 (2007) 1-9.
- [2] Z. Li, S. Zhao, R.O. Ritchie, M.A. Meyers, Mechanical properties of high-entropy alloys with emphasis on face-centered cubic alloys, *Progress in Materials Science* 102 (2019) 296-345.
- [3] Z. Li, K.G. Pradeep, Y. Deng, D. Raabe, C.C. Tasan, Metastable high-entropy dual-phase alloys overcome the strength–ductility trade-off, *Nature* 534(7606) (2016) 227-230.
- [4] K. Ichii, M. Koyama, C.C. Tasan, K. Tsuzaki, Comparative study of hydrogen embrittlement in stable and metastable high-entropy alloys, *Scripta Materialia* 150 (2018) 74-77.
- [5] B. Gludovatz, E.P. George, R.O. Ritchie, Processing, Microstructure and Mechanical Properties of the CrMnFeCoNi High-Entropy Alloy, *JOM* 67(10) (2015) 2262-2270.
- [6] M. Fu, X. Ma, K. Zhao, X. Li, D. Su, High-entropy materials for energy-related applications, *iScience* 24(3) (2021) 102177.
- [7] B. Cantor, I.T.H. Chang, P. Knight, A.J.B. Vincent, Microstructural development in equiatomic multicomponent alloys, *Materials Science and Engineering: A* 375-377 (2004) 213-218.
- [8] A. Gali, E.P. George, Tensile properties of high- and medium-entropy alloys, *Intermetallics* 39 (2013) 74-78.
- [9] F. Otto, A. Dlouhý, C. Somsen, H. Bei, G. Eggeler, E.P. George, The influences of temperature and microstructure on the tensile properties of a CoCrFeMnNi high-entropy alloy, *Acta Materialia* 61(15) (2013) 5743-5755.
- [10] H. Tanimoto, R. Hozumi, M. Kawamura, Electrical resistivity and short-range order in rapid-quenched CrMnFeCoNi high-entropy alloy, *Journal of Alloys and Compounds* 896 (2022) 163059-163059.
- [11] B. Gludovatz, A. Hohenwarter, D. Catoor, H. Chang Edwin, P. George Easo, O. Ritchie Robert, A fracture-resistant high-entropy alloy for cryogenic applications, *Science* 345(6201) (2014) 1153-1158.
- [12] C. Wagner, A. Ferrari, J. Schreuer, J.-P. Couzinié, Y. Ikeda, F. Körmann, G. Eggeler, E.P. George, G. Laplanche, Effects of Cr/Ni ratio on physical properties of Cr-Mn-Fe-Co-Ni high-entropy alloys, *Acta Materialia* 227 (2022) 117693-117693.
- [13] A. Zunger, S.H. Wei, L.G. Ferreira, J.E. Bernard, Special quasirandom structures, *Physical Review Letters* 65(3) (1990) 353-356.
- [14] S. Zhao, G.M. Stocks, Y. Zhang, Stacking fault energies of face-centered cubic concentrated solid solution alloys, *Acta Materialia* 134 (2017) 334-345.
- [15] A.J. Zaddach, C. Niu, C.C. Koch, D.L. Irving, Mechanical Properties and Stacking Fault Energies of NiFeCrCoMn High-Entropy Alloy, *JOM* 65(12) (2013) 1780-1789.

- [16] C. Li, J. Yin, K. Odbadrakh, B.C. Sales, S.J. Zinkle, G.M. Stocks, B.D. Wirth, First principle study of magnetism and vacancy energetics in a near equimolar NiFeMnCr high entropy alloy, *Journal of Applied Physics* 125(15) (2019) 155103.
- [17] E. Osei-Agyemang, G. Balasubramanian, Surface oxidation mechanism of a refractory high-entropy alloy, *npj Materials Degradation* 3(1) (2019) 20.
- [18] S. Wang, T. Zhang, H. Hou, Y. Zhao, The Magnetic, Electronic, and Thermodynamic Properties of High Entropy Alloy CrMnFeCoNi: A First-Principles Study, *physica status solidi (b)* 255(10) (2018) 1800306.
- [19] X. Zhou, W.A. Curtin, First principles study of the effect of hydrogen in austenitic stainless steels and high entropy alloys, *Acta Materialia* 200 (2020) 932-942.
- [20] A. Tamm, A. Aabloo, M. Klintonberg, M. Stocks, A. Caro, Atomic-scale properties of Ni-based FCC ternary, and quaternary alloys, *Acta Materialia* 99 (2015) 307-312.
- [21] J. Ding, Q. Yu, M. Asta, R.O. Ritchie, Tunable stacking fault energies by tailoring local chemical order in CrCoNi medium-entropy alloys, *Proceedings of the National Academy of Sciences* 115(36) (2018) 8919.
- [22] P. Hohenberg, W. Kohn, Inhomogeneous Electron Gas, *Physical Review* 136(3B) (1964) B864--B871.
- [23] W. Kohn, L.J. Sham, Self-Consistent Equations Including Exchange and Correlation Effects, *Physical Review* 140(4A) (1965) A1133--A1138.
- [24] N. Metropolis, A.W. Rosenbluth, M.N. Rosenbluth, A.H. Teller, E. Teller, Equation of State Calculations by Fast Computing Machines, *The Journal of Chemical Physics* 21(6) (1953) 1087-1092.
- [25] F.X. Zhang, S. Zhao, K. Jin, H. Xue, G. Velisa, H. Bei, R. Huang, J.Y.P. Ko, D.C. Pagan, J.C. Neuefeind, W.J. Weber, Y. Zhang, Local Structure and Short-Range Order in a NiCoCr Solid Solution Alloy, *Physical Review Letters* 118(20) (2017).
- [26] R. Zhang, S. Zhao, J. Ding, Y. Chong, T. Jia, C. Ophus, M. Asta, R.O. Ritchie, A.M. Minor, Short-range order and its impact on the CrCoNi medium-entropy alloy, *Nature* 581(7808) (2020) 283-287.
- [27] Q. Ding, Y. Zhang, X. Chen, X. Fu, D. Chen, S. Chen, L. Gu, F. Wei, H. Bei, Y. Gao, M. Wen, J. Li, Z. Zhang, T. Zhu, R.O. Ritchie, Q. Yu, Tuning element distribution, structure and properties by composition in high-entropy alloys, *Nature* 574(7777) (2019) 223-227.
- [28] K.G. Pradeep, N. Wanderka, P. Choi, J. Banhart, B.S. Murty, D. Raabe, Atomic-scale compositional characterization of a nanocrystalline AlCrCuFeNiZn high-entropy alloy using atom probe tomography, *Acta Materialia* 61(12) (2013) 4696-4706.
- [29] M. Laurent-Brocq, A. Akhatova, L. Perrière, S. Chebini, X. Sauvage, E. Leroy, Y. Champion, Insights into the phase diagram of the CrMnFeCoNi high entropy alloy, *Acta Materialia* 88 (2015) 355-365.
- [30] Y. Ma, Q. Wang, C. Li, L.J. Santodonato, M. Feygenson, C. Dong, P.K. Liaw, Chemical short-range orders and the induced structural transition in high-entropy alloys, *Scripta Materialia* 144 (2018) 64-68.
- [31] P. Wang, P. Huang, F.L. Ng, W.J. Sin, S. Lu, M.L.S. Nai, Z. Dong, J. Wei, Additively manufactured CoCrFeNiMn high-entropy alloy via pre-alloyed powder, *Materials & Design* 168 (2019) 107576.

- [32] L. Li, R.D. Kamachali, Z. Li, Z. Zhang, Grain boundary energy effect on grain boundary segregation in an equiatomic high-entropy alloy, *Physical Review Materials* 4(5) (2020) 053603.
- [33] E.J. Pickering, R. Muñoz-Moreno, H.J. Stone, N.G. Jones, Precipitation in the equiatomic high-entropy alloy CrMnFeCoNi, *Scripta Materialia* 113 (2016) 106-109.
- [34] P.F. Yu, L.J. Zhang, H. Cheng, H. Zhang, M.Z. Ma, Y.C. Li, G. Li, P.K. Liaw, R.P. Liu, The high-entropy alloys with high hardness and soft magnetic property prepared by mechanical alloying and high-pressure sintering, *Intermetallics* 70 (2016) 82-87.
- [35] G. Kresse, J. Furthmüller, Efficient iterative schemes for ab initio total-energy calculations using a plane-wave basis set, *Physical Review B* 54(16) (1996) 11169-11186.
- [36] P.E. Blöchl, Projector augmented-wave method, *Physical Review B* 50 (1994) 17953.
- [37] J.P. Perdew, K. Burke, M. Ernzerhof, Generalized gradient approximation made simple, *Physical Review B* 77 (1996) 3865.
- [38] M. Methfessel, A.T. Paxton, High-precision sampling for Brillouin-zone integration in metals, *Physical Review B* 40(6) (1989) 3616-3621.
- [39] J.M. Cowley, An Approximate Theory of Order in Alloys, *Physical Review* 77(5) (1950) 669-675.
- [40] D. de Fontaine, The number of independent pair-correlation functions in multicomponent systems, *Journal of Applied Crystallography* 4(1) (1971) 15-19.
- [41] R. Kikuchi, CVM Entropy Algebra, *Progress of Theoretical Physics Supplement* 115 (1994) 1-26.
- [42] B. Widom, Some Topics in the Theory of Fluids, *The Journal of Chemical Physics* 39(11) (1963) 2808-2812.
- [43] J.B. Piochaud, T.P.C. Klaver, G. Adjanor, P. Olsson, C. Domain, C.S. Becquart, First-principles study of point defects in an fcc Fe-10Ni-20Cr model alloy, *Physical Review B* 89(2) (2014) 24101-24101.
- [44] J.W. Eaton, D. Bateman, S. Hauberg, R. Wehbring, GNU Octave version 5.2.0 manual: a high-level interactive language for numerical computations, 2020.
- [45] T. Williams, C. Kelley, gnuplot, 2021.
- [46] K. Momma, F. Izumi, VESTA 3 for three-dimensional visualization of crystal, volumetric and morphology data, *Journal of Applied Crystallography* 44(6) (2011) 1272-1276.
- [47] B.L. Gyorffy, G.M. Stocks, Concentration Waves and Fermi Surfaces in Random Metallic Alloys, *Physical Review Letters* 50(5) (1983) 374-377.
- [48] P. Singh, A.V. Smirnov, D.D. Johnson, Ta-Nb-Mo-W refractory high-entropy alloys: Anomalous ordering behavior and its intriguing electronic origin, *Physical Review Materials* 2(5) (2018) 055004.
- [49] H.-W. Hsiao, R. Feng, H. Ni, K. An, J.D. Poplawsky, P.K. Liaw, J.-M. Zuo, Data-driven electron-diffraction approach reveals local short-range ordering in CrCoNi with ordering effects, *Nature Communications* 13(1) (2022) 6651.
- [50] C. Niu, A.J. Zaddach, A.A. Oni, X. Sang, J.W. Hurt, J.M. LeBeau, C.C. Koch, D.L. Irving, Spin-driven ordering of Cr in the equiatomic high entropy alloy NiFeCrCo, *Applied Physics Letters* 106(16) (2015) 161906-161906.
- [51] F. Walsh, M. Asta, R.O. Ritchie, Magnetically driven short-range order can explain anomalous measurements in CrCoNi, *Proceedings of the National Academy of Sciences USA* 118(13) (2021) e2020540118-e2020540118.

- [52] N.L. Okamoto, K. Yuge, K. Tanaka, H. Inui, E.P. George, Atomic displacement in the CrMnFeCoNi high-entropy alloy – A scaling factor to predict solid solution strengthening, *AIP Advances* 6(12) (2016) 125008-125008.
- [53] S. Zhao, T. Egami, G.M. Stocks, Y. Zhang, Effect of d electrons on defect properties in equiatomic NiCoCr and NiCoFeCr concentrated solid solution alloys, *Physical Review Materials* 2(1) (2018) 013602.
- [54] B. Schuh, F. Mendez-Martin, B. Völker, E.P. George, H. Clemens, R. Pippan, A. Hohenwarter, Mechanical properties, microstructure and thermal stability of a nanocrystalline CoCrFeMnNi high-entropy alloy after severe plastic deformation, *Acta Materialia* 96 (2015) 258-268.
- [55] J.Y. He, C. Zhu, D.Q. Zhou, W.H. Liu, T.G. Nieh, Z.P. Lu, Steady state flow of the FeCoNiCrMn high entropy alloy at elevated temperatures, *Intermetallics* 55 (2014) 9-14.
- [56] Y.-Y. Li, Quasi-Chemical Method in the Statistical Theory of Regular Mixtures, *Physical Review* 76(7) (1949) 972-979.
- [57] R. Kikuchi, S.G. Brush, Improvement of the Cluster-Variation Method, *The Journal of Chemical Physics* 47(1) (1967) 195-203.
- [58] S.C. Middleburgh, D.M. King, G.R. Lumpkin, M. Cortie, L. Edwards, Segregation and migration of species in the CrCoFeNi high entropy alloy, *Journal of Alloys and Compounds* 599 (2014) 179-182.
- [59] E.W. Huang, H.-S. Chou, K.N. Tu, W.-S. Hung, T.-N. Lam, C.-W. Tsai, C.-Y. Chiang, B.-H. Lin, A.-C. Yeh, S.-H. Chang, Y.-J. Chang, J.-J. Yang, X.-Y. Li, C.-S. Ku, K. An, Y.-W. Chang, Y.-L. Jao, Element Effects on High-Entropy Alloy Vacancy and Heterogeneous Lattice Distortion Subjected to Quasi-equilibrium Heating, *Scientific Reports* 9(1) (2019) 14788.
- [60] M.A. Tschopp, S.P. Coleman, D.L. McDowell, Symmetric and asymmetric tilt grain boundary structure and energy in Cu and Al (and transferability to other fcc metals), *Integrating Materials and Manufacturing Innovation* 4(1) (2015) 176-189.
- [61] L. Li, Z. Li, A. Kwiatkowski da Silva, Z. Peng, H. Zhao, B. Gault, D. Raabe, Segregation-driven grain boundary spinodal decomposition as a pathway for phase nucleation in a high-entropy alloy, *Acta Materialia* 178 (2019) 1-9.
- [62] S.L. Thomas, S. Patala, Vacancy diffusion in multi-principal element alloys: The role of chemical disorder in the ordered lattice, *Acta Materialia* 196 (2020) 144-153.
- [63] M. Vaidya, K.G. Pradeep, B.S. Murty, G. Wilde, S.V. Divinski, Bulk tracer diffusion in CoCrFeNi and CoCrFeMnNi high entropy alloys, *Acta Materialia* 146 (2018) 211-224.
- [64] A.J. Maldonado, K.P. Misra, R.D.K. Misra, Grain boundary segregation in a high entropy alloy, *Materials Technology* 38(1) (2023) 2221959.
- [65] Y. Wu, F. Zhang, X. Yuan, H. Huang, X. Wen, Y. Wang, M. Zhang, H. Wu, X. Liu, H. Wang, S. Jiang, Z. Lu, Short-range ordering and its effects on mechanical properties of high-entropy alloys, *Journal of Materials Science & Technology* 62 (2021) 214-220.
- [66] G. Bracq, J.-C. Crivello, M. Laurent-Brocq, J.-M. Joubert, I. Guillot, What is the Enthalpy Contribution to the Stabilization of the Co–Cr–Fe–Mn–Ni Faced-centered Cubic Solid Solution?, *Journal of Phase Equilibria and Diffusion* 42(5) (2021) 561-570.
- [67] F. Cao, Y. Chen, S. Zhao, E. Ma, L. Dai, Grain boundary phase transformation in a CrCoNi complex concentrated alloy, *Acta Materialia* 209 (2021) 116786.

- [68] X. Zhao, H. Chen, N. Wilson, Q. Liu, J.-F. Nie, Direct observation and impact of co-segregated atoms in magnesium having multiple alloying elements, *Nature Communications* 10(1) (2019) 3243.
- [69] C. Yang, B. Feng, J. Wei, E. Tochigi, S. Ishihara, N. Shibata, Y. Ikuhara, Atomic and electronic band structures of Ti-doped Al₂O₃ grain boundaries, *Acta Materialia* 201 (2020) 488-493.
- [70] E.A. Lazar, J. Han, D.J. Srolovitz, Topological framework for local structure analysis in condensed matter, *Proceedings of the National Academy of Sciences of the United States of America* 112(43) (2015) E5769-E5776.
- [71] H.W. Sheng, W.K. Luo, F.M. Alamgir, J.M. Bai, E. Ma, Atomic packing and short-to-medium-range order in metallic glasses, *Nature* 439(7075) (2006) 419-425.
- [72] Y. Yang, H. Tokunaga, M. Ono, K. Hayashi, J.C. Mauro, Understanding the molar volume of alkali-alkaline earth-silicate glasses via Voronoi polyhedra analysis, *Scripta Materialia* 166 (2019) 1-5.
- [73] B. Yin, S. Yoshida, N. Tsuji, W.A. Curtin, Yield strength and misfit volumes of NiCoCr and implications for short-range-order, *Nature Communications* 11(1) (2020) 2507.